

# Self-healing quantum key distribution using high-dimensional vector modes

ISAAC NAPE,<sup>1</sup> EILEEN OTTE,<sup>2</sup> ADAM VALLÉS,<sup>1,\*</sup> CARMELO ROSALES-GUZMÁN,<sup>1</sup> FILIPPO CARDANO,<sup>3</sup> CORNELIA DENZ,<sup>2</sup>, AND ANDREW FORBES,<sup>1</sup>

<sup>1</sup>*School of Physics, University of the Witwatersrand, Private Bag 3, Wits 2050, South Africa*

<sup>2</sup>*Institute of Applied Physics, University of Muenster, Corrensstr. 2/4, D-48149 Muenster, Germany*

<sup>3</sup>*Dipartimento di Fisica "Ettore Pancini", Università di Napoli Federico II, Complesso Universitario di Monte Sant'Angelo, Via Cinthia, 80126 Napoli, Italy*

*\*adam.vallesmari@wits.ac.za*

## Abstract:

Using spatial modes for quantum key distribution (QKD) has become highly topical due to their infinite dimensionality, promising high information capacity per photon. However, spatial distortion reduce the feasible secret key rates and compromise the security of the quantum channel. In an extreme form, such a distortion would be blocking the channel almost completely with an obstacle. By controlling the radial degree of freedom of a photon's spatial mode, we are able to demonstrate high-dimensional QKD through obstacles with self-reconstructing single photons. We construct high-dimensional mutually unbiased bases using spin-orbit hybrid states that are radially modulated with a non-diffracting Bessel-Gaussian (BG) profile, and show secure transmission through partially obstructed quantum links. Using a prepare-measure protocol we report higher quantum state self-reconstruction and information retention for the non-diffracting BG modes as compared to Laguerre-Gaussian modes, obtaining a quantum bit error rate (QBER) that is up to  $3\times$  lower. This work highlights the importance of controlling the radial mode of single photons in quantum information processing and communication.

© 2024 Optical Society of America under the terms of the [OSA Open Access Publishing Agreement](#)

## 1. Introduction

Quantum key distribution (QKD) enables two parties to securely exchange information detecting the presence of eavesdropping [1]. Unlike conventional cryptography, with unproven computational assumptions, the security of QKD relies on the fundamental laws of quantum mechanics [2], prohibiting the cloning of quantum information encoded in single photons [3]. Although current state of the art implementations have successfully transferred quantum states in free-space [4], optical fibers [5], and between satellites [6], efficient high capacity key generation and robust security are still highly sought-after.

Spatial modes of light hold significant promise in addressing these issues. The channel capacity can be exponentially increased by encoding information in the spatial degree of freedom (DoF) of photons and has been demonstrated with classical light in free-space and fibres [7]. Implementing QKD with high-dimensional (HD) states ( $d > 2$ ) has also been demonstrated [8, 9], by exploiting the ability of each photon to carry up to  $\log_2(d)$  bits per photon while simultaneously increasing the threshold of the quantum bit error rate (QBER). This makes HD QKD protocols more robust [10–12], even when considering extreme perturbing conditions, i.e., underwater submarine communication links [13]. While most studies to date have used spatial modes of light carrying orbital angular momentum (OAM) [14], reaching up to  $d = 7$  [15], higher dimensions are achievable [16–19] with coupled spatial and polarization structures, e.g. vector modes. These states have received considerable attention in both quantum and classical communication (see Ref. [19] for a review) due to their particular advantages such as imple-

menting QKD without a reference frame [20, 21].

To date, there has been only limited work on the impact of perturbations on HD QKD with spatial modes, with most studies considering the decay of two-dimensional spatial mode entanglement in turbulence [22, 23] and only a few addressing the dimensionality issue [24–27]. In turbulence, for example, the key rates are known to decrease [28], with the latter to be compensated for by large OAM states in the superposition.

Here, we take advantage of the self-healing properties in non-diffracting vector beams to show that the bit rate of a QKD channel, affected by partial obstructions, can be ameliorated by encoding information onto diffraction-free single photons. To this end, we generate a non-diffracting (self-reconstructing) set of mutually unbiased bases (MUB), formed by hybrid scalar and vector modes with a Bessel-Gaussian (BG) transverse profile. We herald a single photon with a BG radial profile by means of spontaneous parametric down-conversion (SPDC), generating paired photons and coupling OAM and polarization using a  $q$ -plate [29]. We characterize the quantum link by measuring the scattering probabilities, mutual information and secret key rates in a prepare-measure protocol for BG and Laguerre-Gaussian (LG) photons, comparing the two for various obstacle sizes. We find that the BG modes outperform LG modes for larger obstructions by more than  $3\times$ , highlighting the importance of radial mode control of single photons for quantum information processing and communication.

## 2. Self-healing Bessel modes

Since Bessel modes cannot be realized experimentally, a valid approximation, the Bessel-Gaussian (BG) modes, is commonly used [30]. This approximation inherits from the Bessel modes the ability to self-reconstruct in amplitude, phase [31, 32], and polarization [33–35], even when considering entangled photon pairs [36] or non-separable vector modes [37–39]. Mathematically, they are described by the expression

$$\mathcal{J}_{\ell,k_r}(r, \varphi, z) = \sqrt{\frac{2}{\pi}} J_{\ell} \left( \frac{z_R k_r r}{z_R - iz} \right) \exp(i\ell\varphi - ik_z z) \cdot \exp \left( \frac{ik_r^2 z w_0 - 2kr^2}{4(z_R - iz)} \right), \quad (1)$$

where  $(r, \varphi, z)$  represents the position vector in the cylindrical coordinates,  $\ell$  is the azimuthal index (topological charge). Furthermore,  $J_{\ell}(\cdot)$  defines a Bessel function of the first kind,  $k_r$  and  $k_z$  are the radial and longitudinal components of the wave number  $k = \sqrt{k_r^2 + k_z^2} = 2\pi/\lambda$ . The last factor describes the Gaussian envelope with beam waist  $w_0$  and Rayleigh range  $z_R = \pi w_0^2/\lambda$  for a certain wavelength  $\lambda$ .

The propagation distance over which the BG modes approximate a non-diffracting mode is given by  $z_{\max} = 2\pi w_0/\lambda k_r$  [40]. In the presence of an obstruction of radius  $R$  inserted within the non-diffracting distance, a shadow region of length  $z_{\min} \approx \frac{2\pi R}{k_r \lambda}$  is formed [41]. The distance  $z_{\min}$  determines the minimum distance required for the beam to recover its original form, whereby full reconstruction is achieved at  $2z_{\min}$  [31, 32].

Here, we exploit this property with single photons that have non-separable polarization and OAM DoF. By carefully selecting a  $k_r$  value, we show that the information of single photons encoded with a Bessel spatial profile can be recovered after the shadow region of an obstruction. Next, we introduce a high-dimensional self-healing information basis for QKD, constructed from non-orthogonal vector and scalar BG spatial modes.

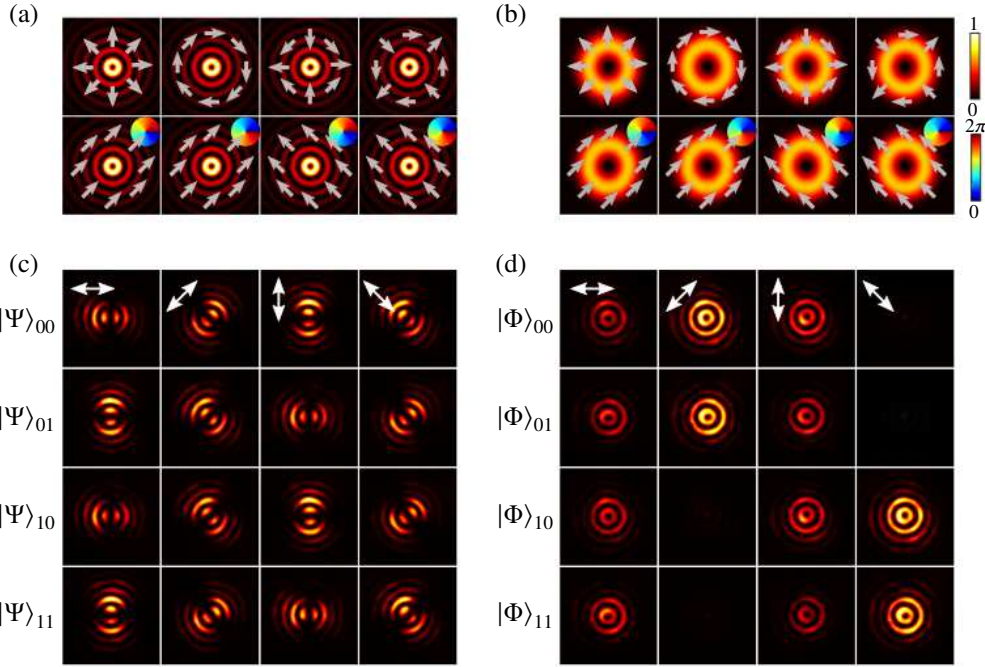


Fig. 1. Intensity and polarization mappings of vector (first row) and scalar (second row) MUB modes with (a) BG and (b) LG radial profiles for  $\ell = \pm 1$ . The polarization projections on the (c) vector  $|\Psi\rangle$  and (d) scalar  $|\Phi\rangle$  basis BG modes. The vector modes have spatially varying polarizations which consequently render the polarization and spatial DoF as non-separable. This is easily seen in the variation of the transverse spatial profile when polarization projections are performed (orientation indicated by white arrow) on the  $|\Psi\rangle$  modes. In contrast, the scalar modes have separable polarization and spatial DoF hence polarization projections only cause fluctuations in the intensity of the transverse profile for the  $|\Phi\rangle$  modes.

### 2.1. Self-healing information basis

In the standard BB84 protocol, Alice and Bob unanimously agree on two information basis. The first basis can be arbitrarily chosen in  $d$  dimensions as  $\{|\psi_i\rangle, i = 1..d\}$ . However, the second basis must fulfill the condition

$$|\langle \psi_i | \phi_j \rangle|^2 = \frac{1}{d}, \quad (2)$$

making  $|\psi\rangle$  and  $|\phi\rangle$  mutually unbiased. Various QKD protocols were first implemented using polarization states, spanned by the canonical right  $|R\rangle$  and left  $|L\rangle$  circular polarization states constituting a two-dimensional Hilbert space, i.e.,  $\mathcal{H}_\sigma = \text{span}\{|L\rangle, |R\rangle\}$ . More dimensions where later realized with the spatial DoF of photons [9, 15], using the OAM DoF spanning the infinite dimensional space, i.e.  $\mathcal{H}_\infty = \bigoplus \mathcal{H}_\ell$ , such that  $\mathcal{H}_\ell = \{|\ell\rangle, |-\ell\rangle\}$  is qubit space characterized by a topological charge  $\pm\ell \in \mathbb{Z}$ .

Here we exploit an even larger encoding state space by combining polarization and OAM,  $\mathcal{H}_\infty = \bigoplus \mathcal{H}_\sigma \otimes \mathcal{H}_\ell$  where  $\mathcal{H}_4 = \mathcal{H}_\sigma \otimes \mathcal{H}_\ell$ , is a qu-quart space spanned by the states  $\{|L\rangle|\ell\rangle, |R\rangle|\ell\rangle, |L\rangle|-\ell\rangle, |R\rangle|-\ell\rangle\}$ , described by the so-called higher-order Poincaré spheres (HOPs) [42, 43]. These modes feature a coupling between polarization and OAM DoF (see Fig. 1(a) for BG and (b) for LG profiles). A high-dimensional information basis with a radially

concentric ring structure of BG modes can be constructed (Fig. 1(a)). Amongst these are the non-separable vector BG modes (Fig. 1(a), first row), known to posses self-reconstruction after encountering obstructions [44].

For this experiment, we chose a mode basis on the  $\mathcal{H}_4$  subspace with  $\ell = \pm 1$ , although, in principle more modes can be used. Our encoding basis is constructed as follows: we define the radial profile  $\mathcal{J}_{\ell,k_r}(r)$  representing the radial component of the BG mode in Eq. (1). Our first mode set is comprised of a self-healing vector BG mode basis, mapped as

$$|\Psi\rangle_{00} = \frac{1}{\sqrt{2}}\mathcal{J}_{\ell,k_r}(r)(|R\rangle|\ell\rangle + |L\rangle|-\ell\rangle), \quad (3)$$

$$|\Psi\rangle_{01} = \frac{1}{\sqrt{2}}\mathcal{J}_{\ell,k_r}(r)(|R\rangle|\ell\rangle - |L\rangle|-\ell\rangle), \quad (4)$$

$$|\Psi\rangle_{10} = \frac{1}{\sqrt{2}}\mathcal{J}_{\ell,k_r}(r)(|L\rangle|\ell\rangle + |R\rangle|-\ell\rangle), \quad (5)$$

$$|\Psi\rangle_{11} = \frac{1}{\sqrt{2}}\mathcal{J}_{\ell,k_r}(r)(|L\rangle|\ell\rangle - |R\rangle|-\ell\rangle), \quad (6)$$

being  $R$  and  $L$  the circular polarization states while  $\ell$  is the topological charge, (see Fig. 1(c) for polarization projections). The second set of orthogonal modes is given by

$$|\Phi\rangle_{00} = \mathcal{J}_{\ell,k_r}(r)|D\rangle|-\ell\rangle, \quad (7)$$

$$|\Phi\rangle_{01} = \mathcal{J}_{\ell,k_r}(r)|D\rangle|\ell\rangle, \quad (8)$$

$$|\Phi\rangle_{10} = \mathcal{J}_{\ell,k_r}(r)|A\rangle|-\ell\rangle, \quad (9)$$

$$|\Phi\rangle_{11} = \mathcal{J}_{\ell,k_r}(r)|A\rangle|\ell\rangle, \quad (10)$$

where  $D$  and  $A$  are the diagonal and anti-diagonal polarization states (see Fig. 1(d) for polarization projections). Conversely, we contrast these MUB modes with an LG vector and scalar MUB by forming an equivalent mode set, i.e, with the same OAM and polarization information but an LG radial profile. The two mode sets are contrasted in Fig. 1(a) and (b). The set  $|\Psi\rangle_{ij}$  and  $|\Phi\rangle_{ij}$  are mutually unbiased and, therefore, form a reputable information basis for QKD in high-dimensions.

### 3. Methods

#### 3.1. Single photon heralding

For unconditional security to be achieved in QKD, a single photon source must be used. However, such sources are yet to be realized, although it is possible to use correlated pairs of photons, where the detection of one photon, the heralding photon, conditions the existence of its correlated pair [45]. Such sources, of heralded single photons, can be produced by means of SPDC. In this process, the statistics of the heralded photon have low multi-photon probabilities.

Thus, we herald a single photon via SPDC where a high frequency photon ( $\lambda = 405$  nm) is absorbed with low probability in a nonlinear crystal, generating a signal ( $s$ ) and idler ( $i$ ) correlated paired photons at  $\lambda = 810$  nm. In the case of a collinear emission of  $s$  and  $i$ , the probability amplitude of detecting mode functions  $|m\rangle_s$  and  $|m\rangle_i$ , respectively, is given by [46]

$$c_{s,i} = \int \int m_s^*(\mathbf{x})m_i^*(\mathbf{x})m_p(\mathbf{x})d^2x, \quad (11)$$

where  $m_p(\mathbf{x})$  is the field profile of the pump ( $p$ ) beam which best approximates the phase-matching condition in the thin crystal limit; the Rayleigh range of the pump beam is much

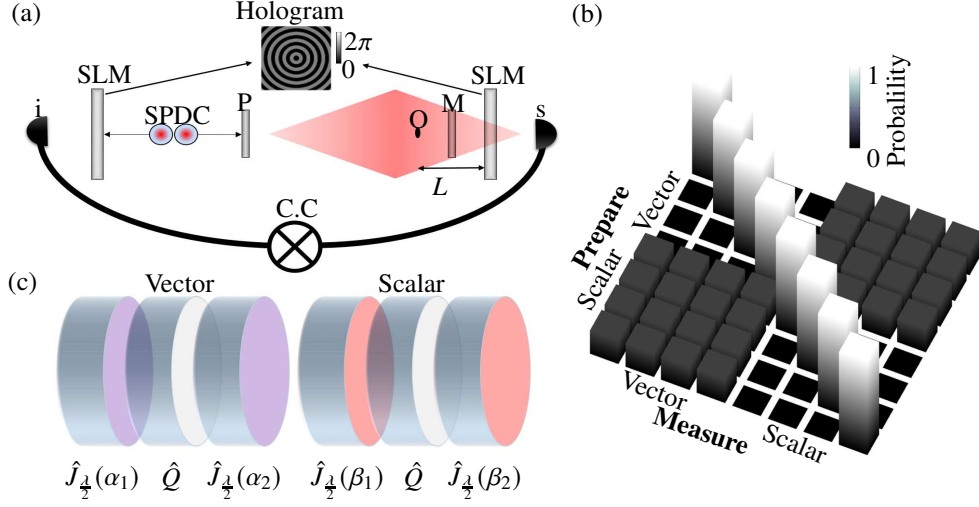


Fig. 2. (a) Conceptual drawing of the QKD with self-healing BG modes. The SLMs post-select the self-healing BG radial profile from the SPDC source. The prepare and measure optics modulate and demodulate the OAM and polarization DoF of the heralded photon. The physical obstruction is placed at a distance  $L$  from the rightmost SLM, which decodes the radial information of Bob's photon. The optics are within  $z_{\max} = 54$  cm distance of the BG modes depicted as the rhombus shape. The propagation of the post-selected BG mode can be determined via back-projection. (b) Optical elements required by Alice and Bob to prepare and measure the spin-coupled states of the heralded photons (cf. Table 1). (c) Numerical scattering probability matrix for the vector and scalar modes sets in free-space. The channels correspond to the probabilities  $|C_{ij}|^2$  calculated from Eq. (22).

larger than the crystal length. The probabilities amplitudes  $c_{s,i}$  can be calculated using the Bessel basis,

$$m_{s,i}(r, \varphi) = \mathcal{J}_{\ell_{s,i}, k_r}(r) \exp(i\ell_{s,i}\varphi), \quad (12)$$

where  $\exp(i\ell\varphi)$  corresponds to the characteristic azimuthal phase mapping onto the state vector  $|\ell\rangle$ . Taking into account a SPDC type-I process and a Gaussian pump beam, the quantum state used to encode and decode the shared key can be written in the Bessel basis as

$$|\Psi\rangle_{AB} = \sum c_{\ell, k_{r,1}, k_{r,2}} |\ell, k_{r,1}\rangle_s |-\ell, k_{r,2}\rangle_i |H\rangle_s |H\rangle_i, \quad (13)$$

being  $|\ell, k_r\rangle_s \sim J_{\ell, k_r}(r) |\ell\rangle$  and  $H$  the horizontal polarization state. The probability amplitudes  $c_{\ell, k_{r,1}, k_{r,2}}$  can be calculated using the overlap integral in Eq. (11). Experimentally  $|c_{\ell, k_{r,1}, k_{r,2}}|^2$  is proportional to the probability of detecting a coincidence when the state  $|\ell, k_{r,1}\rangle_s |-\ell, k_{r,2}\rangle_i$  is selected. Coincidences are optimal when  $|k_{r,1}|$  and  $|k_{r,2}|$  are equivalent.

In this experiment, the idler photon ( $i$ ) is projected into the state  $|0, k_r\rangle_i$ , heralding only the signal photons ( $s$ ) with the same spatial state  $|0, k_r\rangle_s$ , as can be seen in the sketch of Fig. 2(a). Therefore, a prepare-measure protocol can be carried out by using the same  $s$  photon. In other-words, Alice remotely prepares her single photon with a desired radial profile from the SPDC before encoding the polarization and OAM information.

### 3.2. Spatial profile post-selection

Spatial light modulators (SLMs) are a ubiquitous tool for generating and detecting spatial modes [47, 48]. We exploit their on-demand dynamic modulation via computer generated holograms

to post-select the spatial profiles of our desired modes (see hologram inset in Fig. 2(a)). For the detection of BG modes, we choose a binary Bessel function as phase-only hologram, defined by the transmission function

$$T(r, \varphi) = \text{sign}\{J_\ell(k_r r)\} \exp(i\ell\varphi), \quad (14)$$

with the sign function  $\text{sign}\{\cdot\}$  [49,50]. Classically, this approach has the advantage of generating a BG beam immediately after the SLM and, reciprocally, detects the mode efficiently [36]. Importantly, a blazed grating is used to encode the hologram, with the desired mode being detected in the first diffraction order [51] and spatial filtered with a single mode fiber (SMF).

Here, we set  $k_r = 18 \text{ rad/mm}$  and  $\ell = 0$  for the fundamental Bessel mode and, conversely,  $k_r = 0$  to eliminate the multi-ringed Bessel structure.

### 3.3. Mode generation and detection

Liquid crystals  $q$ -plates represent a convenient and versatile way to engineer several types of vector beams [52]. In our setup, vector and scalar modes, described in Fig. 1, are either generated or detected by letting signal photons pass through a combination of these devices and standard wave plates (see Fig. 2(c)). A  $q$ -plate consists of a thin layer of liquid crystals (sandwiched between glass plates) whose optic axes are arranged so that they form a singular pattern with topological charge  $q$  [29]. By adjusting the voltage applied to the plate it is possible to tune its retardation to the optimal value  $\delta = \pi$  [53]. In such a configuration indeed the plate behaves like a standard half-wave plate (with an inhomogeneous orientation of its fast axis) and can be used to change the OAM of circularly polarized light by  $\pm 2q$ , depending on the associated handedness being left or right, respectively. In the Jones matrix formalism, the  $q$ -plate is represented by the operator

$$\hat{Q} = \begin{pmatrix} \cos(2q\varphi) & \sin(2q\varphi) \\ \sin(2q\varphi) & -\cos(2q\varphi) \end{pmatrix} \quad (15)$$

where  $\varphi$  is the azimuthal coordinate. The matrix is then written in the following linear basis

$\{|H\rangle = \begin{pmatrix} 1 \\ 0 \end{pmatrix}, |V\rangle = \begin{pmatrix} 0 \\ 1 \end{pmatrix}\}$ . In our experiment we use  $q$ -plates with  $q = 1/2$ , and half- ( $\frac{1}{2}$ ) as well as quarter-wave plates ( $\frac{1}{4}$ ) for polarization control, represented by the Jones matrices

$$\hat{J}_{\frac{1}{2}}(\theta) = \begin{pmatrix} \cos(2\theta) & \sin(2\theta) \\ \sin(2\theta) & -\cos(2\theta) \end{pmatrix}, \quad (16)$$

and

$$\hat{J}_{\frac{1}{4}}(\theta) = \begin{pmatrix} \cos^2(\theta) + i\sin^2(\theta) & (1-i)\sin(\theta)\cos(\theta) \\ (1-i)\sin(\theta)\cos(\theta) & \sin^2(\theta) + i\cos^2(\theta) \end{pmatrix}. \quad (17)$$

Here,  $\theta$  represents the rotation angle of the wave plates fast axis with respect to the horizontal polarization. The operator associated with the generation of the vector mode is

$$\hat{V}(\alpha_1, \alpha_2) = \hat{J}_{\frac{1}{2}}(\alpha_2) \hat{Q} \hat{J}_{\frac{1}{2}}(\alpha_1) \hat{P}_H, \quad (18)$$

where  $\alpha_1$  and  $\alpha_2$  are the rotation angles for the half-wave plates and  $\hat{P}_H = \begin{pmatrix} 1 & 0 \\ 0 & 0 \end{pmatrix}$  represents the operator for a horizontal linear polarizer. Similarly, the operator for the scalar modes is

$$\hat{S}(\beta_1, \beta_2) = \hat{J}_{\frac{1}{4}}(\beta_2) \hat{Q} \hat{J}_{\frac{1}{4}}(\beta_1) \hat{P}_H, \quad (19)$$

where  $\beta_1$  and  $\beta_2$  are the rotation angles for the quarter-wave plates.

Let the set  $\mathcal{M}_1 = \{\hat{V}_i \mid \hat{V}_i \rightarrow |\psi_i\rangle, i = 1..4\}$  be associated with the generation of vector modes from  $\hat{V}(\alpha_1, \alpha_2)$ , and  $\mathcal{M}_2 = \{\hat{S}_j \mid \hat{S}_j \rightarrow |\phi_j\rangle, j = 1..4\}$  for the scalar modes from  $\hat{S}(\beta_1, \beta_2)$ . The orientation of the angles required to obtain them is given in Table 1 for the vector and scalar modes (see also schematics of wave plates arrangement in Fig. 2(c)).

Table 1. Generation of vector and scalar modes from a horizontally polarized BG mode ( $\ell = 0$ ) at the input. The angles  $\alpha_{1,2}$  and  $\beta_{1,2}$  are defined with respect to the horizontal polarization. For each  $\hat{V}_i$  and  $\hat{S}_i$  we present the angles needed to perform the mapping of  $\mathcal{M}_1 \rightarrow \{|\psi_i\rangle\}$  and  $\mathcal{M}_2 \rightarrow \{|\phi_i\rangle\}$  with a one-to-one correspondence.

Vector ( $\hat{V}(\alpha_1, \alpha_2)$ )			Scalar ( $\hat{S}(\beta_1, \beta_2)$ )		
Operator	$\hat{J}_{\frac{1}{2}}(\alpha_1)$	$\hat{J}_{\frac{1}{2}}(\alpha_2)$	Operator	$\hat{J}_{\frac{1}{4}}(\beta_1)$	$\hat{J}_{\frac{1}{4}}(\beta_2)$
$\hat{V}_1$	0	–	$\hat{S}_1$	$-\pi/4$	0
$\hat{V}_2$	$\pi/4$	–	$\hat{S}_2$	$\pi/4$	$\pi/2$
$\hat{V}_3$	0	0	$\hat{S}_3$	$-\pi/4$	$\pi/2$
$\hat{V}_4$	$\pi/4$	0	$\hat{S}_4$	$\pi/4$	0

### 3.4. Scattering probability

Let  $\hat{A}_i \in \mathcal{M}_1 \cup \mathcal{M}_2$  represent operators selected by Alice and Bob, respectively. Alice first obtains a heralded photon from the SPDC with the input state  $|\psi_{\text{in}}\rangle = \mathcal{J}_{0,k_r} |H\rangle$ . Then, Alice prepares the photon in a desired state from the MUB with

$$|a_i\rangle = \hat{A}_i \mathcal{J}_{0,k_r}(r) |H\rangle. \quad (20)$$

Bob similarly measures the state

$$|b_j\rangle = \hat{B}_j \mathcal{J}_{0,k_r}(r) |H\rangle, \quad (21)$$

where  $\hat{B}_j \in \mathcal{M}_1 \cup \mathcal{M}_2$ . The probability of Bob's detection is

$$C_{ij} = \langle b_j | a_i \rangle = \int_0^{2\pi} \int_0^\infty \langle H | \mathcal{J}_{0,k_r}^*(r) \hat{B}_j^\dagger \hat{A}_i \mathcal{J}_{0,k_r}(r) | H \rangle r dr d\phi. \quad (22)$$

The theoretical probabilities  $|C_{ij}|^2$  are presented in Fig. 2(b).

## 4. Experimental set-up

Figure 3 depicts the experimental setup used to measure the results presented below. The continuous-wave (CW) pumping laser (Cobalt MLD diode laser), centered at  $\lambda = 405$  nm,

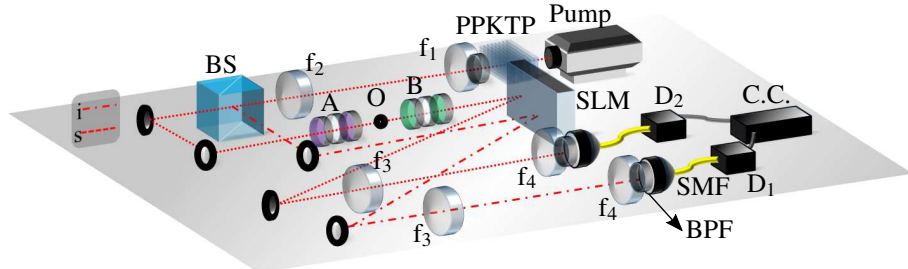


Fig. 3. Experimental setup for the self-healing QKD. Pump:  $\lambda = 405$  nm (Cobalt, MLD laser diode); f: Fourier lenses of focal length  $f_{1,2,3\&4} = 100$  mm, 750 mm, 500 mm, 2 mm, respectively; PPKTP: periodically poled potassium titanyl phosphate (nonlinear crystal); BS: 50:50 beam splitter; s and i: signal and idler photon paths; A: preparation of the state (Alice); O: variable sized obstacle; B: measurement of the state (Bob); SLM: spatial light modulator (Pluto, Holoeye); BPF: band-pass filter; SMF: single mode fiber; D<sub>1&2</sub>: single photon detectors (Perkin Elmer); C.C.: coincidence electronics.

is spatially filtered to clean the beam profile obtaining 40 mW of a 337  $\mu$ m diameter Gaussian beam. This pump beam traverses the temperature controlled 2-mm-long PPKTP nonlinear crystal (Raicol) where photons are absorbed, with low probability, generating two lower-frequency photons (both centered at  $\lambda = 810$  nm) by means of the spontaneous parametric down-conversion (SPDC) process. This particular SPDC process is collinear type-I, meaning that the two lower-frequency photons exiting the nonlinear crystal, signal and idler, have the same linear momentum and horizontal polarization, possessing the temporal correlations needed for the BB84 protocol implementation.

The nonlinear crystal generates the paired photons being able to recreate the non-diffracting length ( $z_{\max}$ ), generating BG modes given a particular post-selected radial wave number. Note that the ( $z_{\max}$ ) distance can be verified by back propagating through the system. We post-selected a wave number of  $k_r = 18$  rad/mm in our case. That is why the crystal plane is relayed with a 4f-system, also relaying the non-diffracting length, having the spatial and polarization projections within the  $z_{\max} = 54$  cm, as schematically shown in Fig. 2(a).

The two paired photons, signal and idler, are spatially separated by a 50:50 beam splitter (BS). The distance between the BS and the SLM are exactly the same for both photon paths. The signal photon, transmitted from the BS, traverses the preparation section (A), where Alice would choose a particular vector or scalar state from the MUB alphabet. The photon encoded with a secure bit is then propagated through the non-diffracting length with self-healing properties, where it encounters a variable sized obstacle. This mimics a real building-to-building quantum channel. The state measurement (B) is implemented right after the obstacle. This simulates Bob's station where particular projections are chosen, from the same MUB that Alice used. The SLM is acting as a horizontal polarization filter, post-selecting the radial wave number defining the  $z_{\max}$  distance. The idler photon, reflected from the BS, is heralding the whole process enabling for the prepare-measure BB84 protocol to be performed.

Subsequently, both photons are properly coupled into single mode fibres (SMF), after being resized by another 4f-system, thus post-selecting the spatial profile by spatial filtering them with the SLM and SMF, and also after being spectrally filtered by a band-pass filter (BPF) with 10 nm bandwidth at full-width at half-maximum (FWHM). The single photon detectors (D<sub>1&2</sub>; Perkin-Elmer) output pulses are then synchronized with a coincidence counter (C.C.), discarding also the cases where the two photons exit the same output port from the BS.

Fig. 4. Crosstalk (scattering) matrix for vector and scalar modes in (a) (I) free-space having post-selected in a BG radial profile. The vector and scalar measured probabilities with the first obstruction (II) having a radius  $R_1 = 600\mu\text{m}$  ( $L > z_{\min}$ ) when taking into account (b) BG and (c) LG radial profiles. Measured probabilities with (III) an obstruction of  $R_2 = 800\mu\text{m}$  ( $L < z_{\min}$ ) when taking into account (d) BG and (e) LG radially profiled single photons.

#### 4.1. Procedure and analysis

We measure the scattering matrix for the BG and, for comparison reasons, the LG profiles under three conditions: (I) in free-space, (II) with a  $R_1 = 600\mu\text{m}$  obstruction placed strategically such that the complete decoding is performed after  $L > z_{\min}$  ( $L$ : distance between obstruction and decoding SLM). Subsequently, (III) with a  $R_2 = 800\mu\text{m}$  obstruction, placed at the same position, however, in this case, the shadow region overlaps the detection system ( $L < z_{\min}$ ). Thus, in the latter case, the mode is not able to self-reconstruct completely before being projected. We measure the quantum bit error ratio (QBER) in each of these cases and computed the mutual information between Alice and Bob in  $d = 4$  dimensions by [11]

$$I_{AB} = \log_2(d) + (1 - e) \log_2(1 - e) + (e) \log_2 \left( \frac{e}{d-1} \right). \quad (23)$$

Here,  $e$  denotes the QBER. Lastly, we measured the practical secure key rate per signal state emitted by Alice, using the Gottesman-Lo-Lütkenhaus-Preskill (GLLP) method [54, 55] for practical implementations with BB84 states, given by

$$R_\Delta = Q_\mu \left( (1 - \Delta) \left( 1 - H_d \left( \frac{e}{1 - \Delta} \right) \right) - f_{\text{EC}} H_d(e) \right), \quad (24)$$

where  $Q_\mu \sim 10^{-4}$  is the photon yield for an average intensity  $\mu$ ,  $H_d(\cdot)$  is the high-dimensional Shannon entropy and  $f_{\text{EC}}$  is a factor that accounts for error correction and is nominally  $f_{\text{EC}} = 1.2$  for error correction systems that are currently in practice. Furthermore,  $\Delta$  is the multi photon rate computed as  $\frac{1 - P_0 - P_1}{Q_\mu}$  where  $P_{0,1}$  are the vacuum and single photon emission probabilities. Moreover the term,  $1 - \Delta$  accounts for photon splitting attacks [55] and can be reduced by using ideal photon sources since  $\Delta \rightarrow 0$ . In our experiment, we measure the photon intensity to be  $\mu = 10^{-3}$  in free-space and decreases accordingly with the varied obstructions.

### 5. Results and Discussion

#### 5.1. Experimental results

We perform a prepare-measure protocol in four dimensions using heralded single photons. The photons are encoded using states from a secure information basis of vector  $|\psi\rangle$  and scalar  $|\phi\rangle$  MUB modes. We change between BG and LG (with a radial index  $p = 0$ , i.e. with no concentric rings) spatial profiles and compare their performance under the influence of varying sized obstructions. Accordingly, the reconstruction distance for both radial profiles, varied the levels of noise at the SLM plane. We subsequently measure the QBER ( $e$ ) and security parameters.

We present the measured detection probability matrices for three tested cases in Fig. 4: (a) free-space; (b) and (c) when the single photon is perturbed and subsequently self-constructed (i.e. with  $R_1 = 600\mu\text{m}$ ,  $L > z_{\min}$ ) for BG and LG modes, respectively; and (d) and (e) when reconstruction is not yet complete (with  $R_2 = 800\mu\text{m}$ ,  $L < z_{\min}$ ), i.e., the shadow of the obstruction overlaps the detection system for BG and LG modes, respectively. In the free-space case, we measure QBERs of  $e = 0.04 \pm 0.004$  for the BG and LG spatial profiles (see Fig. 4(a) and Table 2). We compute a mutual information of  $I_{AB} = 1.69$  bits/photon and a secure key rate of  $R_\Delta/Q_\mu = (1.38)$  bits/s per photon for both radial profiles.

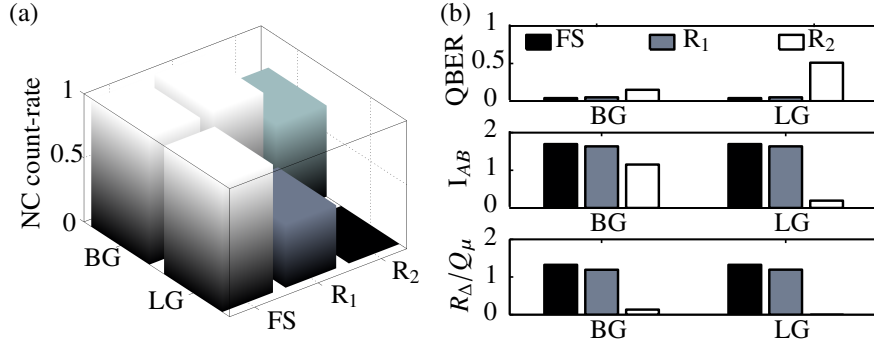


Fig. 5. (a) Experimental normalized coincidence (NC) count-rate for the BG and LG MUB for free-space (FS) and the two obstructions ( $R_1 = 600 \mu\text{m}$  and  $R_2 = 800 \mu\text{m}$ ) on the radially polarized mode  $|\psi\rangle_{00}$ . (b) The QBER, mutual information ( $I_{AB}$ ) and key rate ( $R_\Delta/Q_\mu$ ) for the BG and LG modes with no perturbation and under the two tested obstructions are shown.

Under the perturbation of the  $R_1 = 600 \mu\text{m}$  obstruction, we measure a QBER of  $e = 0.05$  for both spatial profiles, indicative of information retention, i.e. high fidelity. The intensity fields from the back-projected classical beam (see insets of Fig. 4(b) and (c)), show self-healing of the BG mode at the SLM plane (see Fig. 4(b)), although the LG is not completely reconstructed (see Fig. 4(c)). The photons encoded with the LG profile may have a large component of the input mode which is undisturbed in polarization and phase. Furthermore, the photon counts decrease to 49% for the LG profile relative to the counts in free-space, as highlighted in Fig. 5(a). In comparison, the BG modes retain the same intensity thanks to the multiple concentric rings.

Lastly, we investigate the security when the  $R_2 = 800 \mu\text{m}$  obstruction is used. Remarkably, as illustrated in Fig. 5(a), the signal decreased by almost four orders of magnitude, remaining only the 0.07% of the signal for the LG set, but up to 71% for the BG self-healing mode set, owing to an earlier reconstruction of the BG radial profile in comparison to the LG radial profile. Based on the measurement results shown in Fig. 4(d) and (e), we determine a QBER of  $e = 0.15 \pm 0.01$  and  $e = 0.51 \pm 0.00$  for the BG and LG modes, respectively. The mutual information ( $I_{AB}$ ) and secure key rates are higher for the BG basis than the LG, even though the BG MUB has not fully reconstructed (see Fig. 5(b)). In total, see Table 2 for the summarized measured security parameters of the BG and LG mode sets.

### 5.2. Security of high-dimensional self-reconstructing modes

We have presented a *proof-of-concept* experiment showing the advantage of using BG self-healing, high-dimensional states, to encode information in both, the OAM and polarization DoFs. Our scheme shows that with high-dimensional encoding and self-reconstruction, high information transmission rates in quantum communication coupled with the added improvement to the security [11] are achievable.

Our scheme exploits the radial DoF which has previously not been used in high-dimensional QKD implementations with spatial modes. All previous reports only exploited either the OAM or spin-orbit coupled DoF. Our scheme outperforms these previous implementations since no provision for channel losses due to obstructions have been made and with the aid of self-reconstruction, channel perturbations can be alleviated.

Furthermore, we stress that although there are reported benefits with using HD encoding,

Table 2. Measured security parameters for the self-healing BG (LG) modes. NC represents the normalized coincidence counts. The normalization was performed with respect to the counts obtained from the free-space measurements.

BG (LG) modes			
	Free-space	$R_1 = 600 \mu\text{m}$	$R_2 = 800 \mu\text{m}$
QBER	$0.04 \pm 0.01 (0.04 \pm 0.01)$	$0.05 \pm 0.02 (0.05 \pm 0.03)$	$0.15 \pm 0.01 (0.51 \pm 0.00)$
$I_{AB}$	$1.69 \pm 0.06 (1.69 \pm 0.03)$	$1.63 \pm 0.1 (1.63 \pm 0.02)$	$1.15 \pm 0.4 (0.19 \pm 0.04)$
$\Delta$	$2.00 \cdot 10^{-3} (2.00 \cdot 10^{-3})$	$2.00 \cdot 10^{-3} (0.92 \cdot 10^{-3})$	$1.40 \cdot 10^{-3} (0.00)$
$\frac{R_\Delta}{Q_\mu}$	$1.32 \pm 0.06 (1.32 \pm 0.03)$	$1.19 \pm 0.1 (1.19 \pm 0.02)$	$0.13 \pm 0.4 (0.01 \pm 0.00)$
NC	$1 \pm 0.01 (1 \pm 0.00)$	$1 \pm 0.02 (0.49 \pm 0.00)$	$0.71 \pm 0.01 (0.0 \pm 0.00)$

not all protocols have been generalized to high-dimensions, for example, the SARG04 protocol [56] which is designed for robustness against the photon number splitting attacks or the B92 protocol which is a simpler version of the BB84 protocol [57]. Alternatively, decoy states can be implemented with the BB84 states and there have been various reports with HD encoding using spatial modes in free-space and fiber [58, 59]. Another alternative is the KMB09 protocol [60–62]. The security of the scheme is due to a minimum index transmission error rate (ITER) and quantum bit error rate (QBER) introduced by an eavesdropper. The ITER increase significantly for higher dimensional photon states allowing for more noise in the transmission line. Using HD self-healing spatial modes could improve the performance of such protocols in free-space and overcome some of the practical difficulties that are faced when using the transverse spatial modes of photons.

Although the scheme we present is filter based, i.e. filtering states one at a time, we stress that the experiment can be performed robustly and more efficiently using a deterministic detector for spin-orbit coupled states, sorting the modes in position [19]. This ensures high detection rates. Obtaining high switching between modes during generation may require fast modulators which is a serious experimental challenge when implementing HD QKD [63].

## 6. Conclusion

The self-healing property of the Bessel-Gaussian modes opens an important research field, being able to securely share the cryptographic key despite any possible obstruction partially blocking the quantum channel. We have shown in this manuscript the experimental results of the scattering probabilities, mutual information and secret key rates in a prepare-measure protocol, comparing two different modes forming the QKD quantum state alphabet: Bessel-Gaussian (BG) and Laguerre-Gaussian (LG). Our results clearly show lower quantum bit error rate (QBER) by using BG modes when transmitting the shared key through a mostly blocked quantum channel. Concretely, we measured a QBER of  $0.15 \pm 0.01$  and  $0.51 \pm 0.00$  for the BG and LG modes, respectively. Furthermore, when almost completely blocking the channel, the mutual information for the BG modes only drops due to the increase of the noise with respect of the signal. The quantum state information can be reconstructed even when having barely any photons after the obstacle.

## Acknowledgments

The authors express their gratitude to Lorenzo Marrucci and Bruno Piccirillo for providing the  $q$ -plates. I.N., E.O., A.V. and F.C. acknowledge financial support from the Department of Science and Technology (South Africa), the German Research Foundation (DFG; DE-486-22, TRR61), the Claude Leon Foundation and the European Research Council (ERC), under Grant No. 694683 (PHOSPhOR), respectively.

## References

1. H. Bennett Ch and G. Brassard, “Quantum cryptography: public key distribution and coin tossing int,” in *Conf. on Computers, Systems and Signal Processing (Bangalore, India, Dec. 1984)*, (1984), pp. 175–9.
2. P. W. Shor and J. Preskill, “Simple proof of security of the bb84 quantum key distribution protocol,” *Phys. review letters* **85**, 441 (2000).
3. W. K. Wootters and W. H. Zurek, “A single quantum cannot be cloned,” *Nature* **299**, 802–803 (1982).
4. T. Schmitt-Manderbach, H. Weier, M. Fürst, R. Ursin, F. Tiefenbacher, T. Scheidl, J. Perdigues, Z. Sodnik, C. Kurt-siefer, J. G. Rarity *et al.*, “Experimental demonstration of free-space decoy-state quantum key distribution over 144 km,” *Phys. Rev. Lett.* **98**, 010504 (2007).
5. C. Gobby, Z. Yuan, and A. Shields, “Quantum key distribution over 122 km of standard telecom fiber,” *Appl. Phys. Lett.* **84**, 3762–3764 (2004).
6. S.-K. Liao, W.-Q. Cai, W.-Y. Liu, L. Zhang, Y. Li, J.-G. Ren, J. Yin, Q. Shen, Y. Cao, Z.-P. Li *et al.*, “Satellite-to-ground quantum key distribution,” *Nature* **549**, 43 (2017).
7. N. Bozinovic, Y. Yue, Y. Ren, M. Tur, P. Kristensen, H. Huang, A. E. Willner, and S. Ramachandran, “Terabit-scale orbital angular momentum mode division multiplexing in fibers,” *science* **340**, 1545–1548 (2013).
8. S. Gröblacher, T. Jennewein, A. Vaziri, G. Weihs, and A. Zeilinger, “Experimental quantum cryptography with qutrits,” *New J. Phys.* **8**, 75 (2006).
9. M. Mafu, A. Dudley, S. Goyal, D. Giovannini, M. McLaren, M. J. Padgett, T. Konrad, F. Petruccione, N. Lütkenhaus, and A. Forbes, “Higher-dimensional orbital-angular-momentum-based quantum key distribution with mutually unbiased bases,” *Phys. Rev. A* **88**, 032305 (2013).
10. H. Bechmann-Pasquinucci and W. Tittel, “Quantum cryptography using larger alphabets,” *Phys. Rev. A* **61**, 062308 (2000).
11. N. J. Cerf, M. Bourennane, A. Karlsson, and N. Gisin, “Security of quantum key distribution using d-level systems,” *Phys. Rev. Lett.* **88**, 127902 (2002).
12. I. Ali-Khan, C. J. Broadbent, and J. C. Howell, “Large-alphabet quantum key distribution using energy-time entangled bipartite states,” *Phys. review letters* **98**, 060503 (2007).
13. F. Bouchard, A. Sit, F. Hufnagel, A. Abbas, Y. Zhang, K. Heshami, R. Fickler, C. Marquardt, G. Leuchs, R. W. Boyd *et al.*, “Underwater quantum key distribution in outdoor conditions with twisted photons,” *arXiv preprint arXiv:1801.10299* (2018).
14. G. Molina-Terriza, J. P. Torres, and L. Torner, “Twisted photons,” *Nat. physics* **3**, 305 (2007).
15. M. Mirhosseini, O. S. Magaña-Loaiza, M. N. O’Sullivan, B. Rodenburg, M. Malik, M. P. Lavery, M. J. Padgett, D. J. Gauthier, and R. W. Boyd, “High-dimensional quantum cryptography with twisted light,” *New J. Phys.* **17**, 033033 (2015).
16. G. Milione, T. A. Nguyen, J. Leach, D. A. Nolan, and R. R. Alfano, “Using the nonseparability of vector beams to encode information for optical communication,” *Opt. Lett.* **40**, 4887 (2015).
17. P. Li, B. Wang, and X. Zhang, “High-dimensional encoding based on classical nonseparability,” *Opt. Express* **24**, 15143 (2016).
18. G. Milione, M. P. J. Lavery, H. Huang, Y. Ren, G. Xie, T. A. Nguyen, E. Karimi, L. Marrucci, D. A. Nolan, R. R. Alfano, and A. E. Willner, “4  $\times$  20 Gbit/s mode division multiplexing over free space using vector modes and a  $q$ -plate mode (de)multiplexer,” *Opt. letters* **40**, 1980–3 (2015).
19. B. Ndagano, I. Nape, M. A. Cox, C. Rosales-Guzman, and A. Forbes, “Creation and detection of vector vortex modes for classical and quantum communication,” *J. Light. Technol.* **36**, 292–301 (2018).
20. C. Souza, C. Borges, a. Khouri, J. Huguenin, L. Aolita, and S. Walborn, “Quantum key distribution without a shared reference frame,” *Phys. Rev. A* **77**, 1–4 (2008).
21. G. Vallone, V. D’Ambrosio, A. Sponselli, S. Slussarenko, L. Marrucci, F. Sciarrino, and P. Villoresi, “Free-space quantum key distribution by rotation-invariant twisted photons,” *Phys. review letters* **113**, 060503 (2014).
22. A. H. Ibrahim, F. S. Roux, M. McLaren, T. Konrad, and A. Forbes, “Orbital-angular-momentum entanglement in turbulence,” *Phys. Rev. A* **88**, 012312 (2013).
23. F. S. Roux, T. Wellens, and V. N. Shatokhin, “Entanglement evolution of twisted photons in strong atmospheric turbulence,” *Phys. Rev. A* **92**, 012326 (2015).
24. M. Huber and M. Pawłowski, “Weak randomness in device-independent quantum key distribution and the advantage of using high-dimensional entanglement,” *Phys. Rev. A* **88**, 032309 (2013).
25. M. Krenn, R. Fickler, M. Fink, J. Handsteiner, M. Malik, T. Scheidl, R. Ursin, and A. Zeilinger, “Communication with spatially modulated light through turbulent air across vienna,” *New J. Phys.* **16**, 113028 (2014).

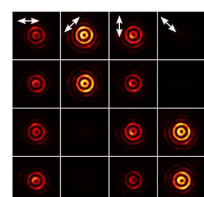
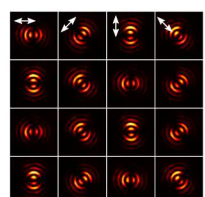
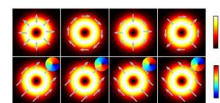
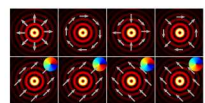
26. A. Sit, F. Bouchard, R. Fickler, J. Gagnon-Bischoff, H. Larocque, K. Heshami, D. Elser, C. Peuntinger, K. Günthner, B. Heim *et al.*, “High-dimensional intracity quantum cryptography with structured photons,” *Optica* **4**, 1006–1010 (2017).
27. M. P. Lavery, C. Peuntinger, K. Günthner, P. Banzer, D. Elser, R. W. Boyd, M. J. Padgett, C. Marquardt, and G. Leuchs, “Free-space propagation of high-dimensional structured optical fields in an urban environment,” *Sci. Adv.* **3**, e1700552 (2017).
28. C. Erven, B. Heim, E. Meyer-Scott, J. Bourgoin, R. Laflamme, G. Weihs, and T. Jennewein, “Studying free-space transmission statistics and improving free-space quantum key distribution in the turbulent atmosphere,” *New J. Phys.* **14**, 123018 (2012).
29. L. Marrucci, C. Manzo, and D. Paparo, “Optical Spin-to-Orbital Angular Momentum Conversion in Inhomogeneous Anisotropic Media,” *Phys. Rev. Lett.* **96**, 163905 (2006).
30. F. Gori, G. Guattari, and C. Padovani, “Bessel-gauss beams,” *Opt. Commun.* **64**, 491 – 495 (1987).
31. D. McGloin, V. Garcés-Chávez, and K. Dholakia, “Interfering bessel beams for optical micromanipulation,” *Opt. Lett.* **28**, 657–659 (2003).
32. I. A. Litvin, M. G. McLaren, and A. Forbes, “A conical wave approach to calculating bessel–gauss beam reconstruction after complex obstacles,” *Opt. Commun.* **282**, 1078 – 1082 (2009).
33. G. Milione, A. Dudley, T. A. Nguyen, O. Chakraborty, E. Karimi, A. Forbes, and R. R. Alfano, “Measuring the self-healing of the spatially inhomogeneous states of polarization of vector bessel beams,” *J. Opt.* **17**, 035617 (2015).
34. G. Wu, F. Wang, and Y. Cai, “Generation and self-healing of a radially polarized bessel-gauss beam,” *Phys. Rev. A* **89**, 043807 (2014).
35. P. Li, Y. Zhang, S. Liu, H. Cheng, L. Han, D. Wu, and J. Zhao, “Generation and self-healing of vector bessel-gauss beams with variant state of polarizations upon propagation,” *Opt. Express* **25**, 5821–5831 (2017).
36. M. McLaren, T. Mhlanya, M. J. Padgett, F. S. Roux, and A. Forbes, “Self-healing of quantum entanglement after an obstruction,” *Nat. Commun.* **5**, 3248 EP – (2014).
37. E. Otte, I. Nape, C. Rosales-Guzmán, A. Vallés, C. Denz, and A. Forbes, “Recovery of local entanglement in self-healing vector vortex bessel beams,” *arXiv preprint arXiv:1805.08179* (2018).
38. C. Rosales-Guzmán, N. Bhebhe, and A. Forbes, “Simultaneous generation of multiple vector beams on a single slm,” *Opt. Express* **25**, 25697–25706 (2017).
39. E. Otte, C. Rosales-Guzmán, B. Ndagano, C. Denz, and A. Forbes, “Entanglement beating in free space through spin-orbit coupling,” *Light. Sci. & Appl.* **7**, e18009 (2018).
40. M. Lapointe, “Review of non-diffracting Bessel beam experiments,” *Opt. & Laser Technol.* **24**, 315–321 (1992).
41. Z. Bouchal, J. Wagner, and M. Chlup, “Self-reconstruction of a distorted nondiffracting beam,” *Opt. Commun.* **151**, 207 – 211 (1998).
42. G. Milione, H. I. Sztul, D. a. Nolan, and R. R. Alfano, “Higher-Order Poincaré Sphere, Stokes Parameters, and the Angular Momentum of Light,” *Phys. Rev. Lett.* **107**, 053601 (2011).
43. A. Holleczeck, A. Aiello, C. Gabriel, C. Marquardt, and G. Leuchs, “Classical and quantum properties of cylindrically polarized states of light,” *Opt. express* **19**, 9714–9736 (2011).
44. G. Milione, A. Dudley, T. A. Nguyen, O. Chakraborty, E. Karimi, A. Forbes, and R. R. Alfano, “Measuring the self-healing of the spatially inhomogeneous states of polarization of vector bessel beams,” *J. Opt.* **17**, 035617 (2015).
45. M. Eisaman, J. Fan, A. Migdall, and S. V. Polyakov, “Invited review article: Single-photon sources and detectors,” *Rev. scientific instruments* **82**, 071101 (2011).
46. Y. Zhang, M. McLaren, F. S. Roux, and A. Forbes, “Simulating quantum state engineering in spontaneous parametric down-conversion using classical light,” *Opt. express* **22**, 17039–17049 (2014).
47. C. Rosales-Guzmán and A. Forbes, *How to shape light with spatial light modulators* (SPIE Press, 2017).
48. A. Forbes, A. Dudley, and M. McLaren, “Creation and detection of optical modes with spatial light modulators,” *Adv. Opt. Photonics* **8**, 200 (2016).
49. J. Turunen, A. Vasara, and A. T. Friberg, “Holographic generation of diffraction-free beams,” *Appl. Opt.* **27**, 3959–3962 (1988).
50. D. M. Cottrell, J. M. Craven, and J. A. Davis, “Nondiffracting random intensity patterns,” *Opt. Lett.* **32**, 298–300 (2007).
51. J. A. Davis, D. M. Cottrell, J. Campos, M. J. Yzuel, and I. Moreno, “Encoding amplitude information onto phase-only filters,” *Appl. Opt.* **38**, 5004–5013 (1999).
52. F. Cardano, E. Karimi, S. Slussarenko, L. Marrucci, C. de Lisio, and E. Santamato, “Polarization pattern of vector vortex beams generated by q-plates with different topological charges,” *Appl. Opt.* **51**, C1–C6 (2012).
53. B. Piccirillo, V. D’Ambrosio, S. Slussarenko, L. Marrucci, and E. Santamato, “Photon spin-to-orbital angular momentum conversion via an electrically tunable q-plate,” *Appl. Phys. Lett.* **97**, 241104 (2010).
54. D. Gottesman and H. Lo, “D. gottesman, h.-k. lo, n. lütkenhaus, and j. preskill, quantum inf. comput. 4, 325 (2004).” *Quantum Inf. Comput.* **4**, 325 (2004).
55. M. Schiavon, G. Vallone, F. Ticozzi, and P. Villoresi, “Heralded single-photon sources for quantum-key-distribution applications,” *Phys. Rev. A* **93**, 012331 (2016).
56. V. Scarani, A. Acin, G. Ribordy, and N. Gisin, “Quantum cryptography protocols robust against photon number splitting attacks for weak laser pulse implementations,” *Phys. review letters* **92**, 057901 (2004).
57. H. Singh, D. Gupta, and A. Singh, “Quantum key distribution protocols: a review,” *IOSR J. Comput. Eng. (IOSR-*

JCE) **16** (2014).

- 58. S. Etcheverry, G. Cañas, E. Gómez, W. Nogueira, C. Saavedra, G. Xavier, and G. Lima, “Quantum key distribution session with 16-dimensional photonic states,” *Sci. reports* **3**, 2316 (2013).
- 59. G. Cañas, N. Vera, J. Cariñe, P. González, J. Cardenas, P. Connolly, A. Przysiezna, E. Gómez, M. Figueroa, G. Vallone *et al.*, “High-dimensional decoy-state quantum key distribution over multicore telecommunication fibers,” *Phys. Rev. A* **96**, 022317 (2017).
- 60. M. M. Khan, M. Murphy, and A. Beige, “High error-rate quantum key distribution for long-distance communication,” *New J. Phys.* **11**, 063043 (2009).
- 61. M. Lopes and N. Sarwade, “On the performance of quantum cryptographic protocols sarg04 and kmb09,” in *Communication, Information & Computing Technology (ICCICT), 2015 International Conference on*, (IEEE, 2015), pp. 1–6.
- 62. M. M. Khan, J. Xu, and A. Beige, “A detailed analysis of kmb09 qkd protocol,” *Int. J. Comput. Sci. Inf. Secur.* **15**, 529 (2017).
- 63. E. Diamanti, H.-K. Lo, B. Qi, and Z. Yuan, “Practical challenges in quantum key distribution,” *npj Quantum Inf.* **2**, 16025 (2016).

This figure "CrosstalkMatrix.png" is available in "png" format from:

<http://arxiv.org/ps/1806.11062v1>





This figure "NormCoin.png" is available in "png" format from:

<http://arxiv.org/ps/1806.11062v1>

